Light-induced deformation and instability of a liquid interface. II. Dynamics

Régis Wunenburger,* Alexis Casner,† and Jean-Pierre Delville‡
Centre de Physique Moléculaire Optique et Hertzienne, Université Bordeaux I, 351 cours de la Libération, 33405 Talence Cedex, France
(Received 15 June 2005; published 27 March 2006)

We study the dynamics of the deformation of a soft liquid-liquid interface by the optical radiation pressure of a focused cw Gaussian laser beam. We measured the temporal evolution of both the hump height and the hump curvature by direct observation and by detecting the focusing effect of the hump acting as a lens. Extending the results of Yoshitake *et al.* [J. Appl. Phys. **97**, 024901 (2005)] to the case of liquid-liquid interfaces and to the $\mathrm{Bo}\simeq 1$ regime [$\mathrm{Bo}=(\omega_0/\ell_c)^2$, where ω_0 is the beam waist and ℓ_c the capillary length], we show that, in the $\mathrm{Bo}\ll 1$ and $\mathrm{Bo}\simeq 1$ ranges, the small-amplitude deformations are correctly described by a linear hydrodynamic theory predicting an overdamped dynamics. We also study the dynamics of the large-amplitude interface deformations at the onset of optohydrodynamic instability [Phys. Rev. Lett. **90**, 144503 (2003)]. Using a simple, phenomenological model for the nonlinear evolution of the hump height, we interpret the observed interface dynamics at the instability onset as the signature of an imperfect subcritical instability.

DOI: 10.1103/PhysRevE.73.036315 PACS number(s): 47.20.Ma, 42.50.Vk, 68.05.−n, 68.03.Kn

I. INTRODUCTION

First attempts at the observation of measurable liquid interface deformations by laser waves were performed with fairly high-energy laser pulses [1–3] because the transfer of photon momentum to a dielectric interface is intrinsically weak and the corresponding pressure, which is proportional to the index contrast and the beam intensity, pushes against the Laplace pressure associated with interfacial tension. For example, Ashkin and Dziedzic [1] performed an experiment using a frequency-doubled Nd:YAG laser (wavelength in vacuum $\lambda_0=0.53$ μm) strongly focused on the water free surface (beam waist value $\omega_0=2.1$ μm). Due to the large value of the water-air surface tension ($\sigma=73$ mJ m^{-2}), they worked with laser pulses (pulse duration 60 ns and peak power between 1 and 4 kW) to increase radiation pressure effects by compensating the weakness of the index contrast by the beam intensity. The interface bending was still very weak (typically a few hundreds of nanometers in height). Similarly, to observe interface disruption, Zhang and Chang [2] considered the incident radiation from a flashlamp-pumped dye laser emitting at $\lambda=0.6$ μm with a spot diameter of ~ 200 μm, a pulse duration of 400 ns and an energy varying between 100 and 200 mJ. Both examples raised an important property of radiation pressure effects. With classical fluids, the time scale associated with the growth rate of the interface deformation is of the order of a few hundreds of nanoseconds (typically 400 ns and 4 μs, respectively, for the Ashkin-Dziedzic and Zhang-Chang conditions). Since interface deformation also means lensing [1,4], these experiments strongly suggest a way to build adaptive optical blocks with fast switching response such as microlenses. That is why radiation pressure effects produced by pulsed lasers were extended to the recording of dynamic holograms [3]. Compared to thermally driven surface relief distortions caused by surface tension gradients (also called Marangoni or thermo capillary deformations [5,6]), which are used for infrared imaging [7] and hologram writing too [8], nonthermal deformations produced by the radiation pressure have two main advantages: (i) energy is not dissipated and (ii) the recording and the erasure rate are not determined by mass and thermal transport over the entire fluid layer (i.e., the rates do not depend on the thickness of the sample). However, even if all these experiments clearly illustrate the potentialities of radiation pressure effects in terms of adaptive optical addressing, they present a major drawback. The high radiation intensities needed to noticeably deform interfaces require reasonably short pulses, typically less than or of the order of a few hundreds of nanoseconds as in the experiments presented above. Consequently, the response time of the fluid interface is always much longer than the pulse duration. This prevents investigations of the entire dynamics of a fully developed deformation; this dynamics is always truncated. Moreover, to reach high beam intensities, *Q*-switched lasers were commonly used. The resulting amplification of the irradiance leads to pulses of complex shape which are difficult to characterize while the spatio temporal profile of the wave is crucial for the calculation of the radiation pressure and the resulting interface deformation. That is why recent investigations of interface deformations by the radiation pressure considered instead continuous laser waves which were further modulated temporally. The main drawback is that interface deformations become too weak to be directly observed. This is certainly the reason why so few works were dedicated to radiation pressure, even if the Ashkin-Dziedzic adaptive lensing method offers sufficiently valuable sensitivity for the detection of the induced nanometric bulge and further quantitative measurements. However, the 1980s have seen the emergence of so-called soft matter physics, which brought a sort of renewal to the concept of laser radiation pressure by opening new horizons beyond the optical physics area. For example, Sakai *et al.* [9] showed

*Electronic address: r.wunenburger@cpmoh.u-bordeaux1.fr
†Present address: CEA/DAM Ile-de-France, BP 12, F-91680 Bruyères-le-Châtel, France. Electronic address: alexis.casner@cea.fr
‡Electronic address: jp.delville@cpmoh.u-bordeaux1.fr

how periodic radiation pressure can control the excitation of capillary waves and how the characterization of their dynamics can be used to deduce surface or bulk properties such as surface tension and low-amplitude shear viscosities. The key point here is the contactless property of the method which allows for *in situ* measurements and prevents mechanical contact with fluid surfaces as well as possible chemical contamination by these mechanical disturbances. This dynamical approach was further extended to the difficult problem of the quantitative measurements of high-viscosity systems [10]. The advantage here is the rapidity of measurements (typically a few seconds) associated with the fact that the viscous motion of the fluid is limited to the microscopic volume excited by the laser beam.

Improvements in these applications, for instance, require an experimental confrontation to the different dynamic regimes that are expected to depend on the competition between capillary waves and overdamped modes resulting from viscous dissipation. While now the efficiency of the technique is well established in several conditions, the demonstration of its versatility still deserves further developments because it appears that there are several regimes in interface deformation that have not been studied yet. For example, buoyancy effects were neglected in the experiments presented above. If such an assumption is realistic for the usual fluids, for which the surface tension of the free surface is generally large, it is not necessarily true when surfactants are present at the interface between two fluids as in complex fluids. As illustrated in the following, the equation describing the dynamics of laser-induced interface deformations includes both properties of the fluids used (the density contrast at the interface in the hydrostatic pressure term, the surface tension in the Laplace pressure, and the shear viscosity in the dynamic viscous pressure) and external optical parameters, such as the beam power and the beam waist. This gives us the opportunity to build new dimensionless quantities, such as an optical Bond number Bo which takes into account the coupling and competition between the characteristic length scale of the optical excitation and that of the fluid interface. We showed that stationary deformations can be described by a universal function of Bo [11]. This function presents two asymptotic regimes. Depending on whether $\mathrm{Bo} \ll 1$ (case of usual fluids) or $\mathrm{Bo} \gg 1$ (when surface tension effects are dominated by buoyancy), we showed in the preceding companion article [12] that stationary deformations are described by different universal behaviors.

In the present investigation, we extend this approach to a description of the dynamics of interface deformations driven by the radiation pressure. Moreover, beyond our analysis of the linear regime (deformations of small amplitude) in terms of scaled behavior, our knowledge of nonlinear interface deformations, which appear at high laser irradiance, is scarce. Since the publication, more than 15 years ago by Zhang and Chang [2] of impressive pictures of the dynamics of droplet disruption driven by laser pulses, almost nothing has been presented in this direction, except three theoretical descriptions of the weakly nonlinear regime of deformation [13–15]. Based on linear-wave theory, they cannot, nevertheless, explain giant deformations as well as the subsequent droplet disruption. In the preceding companion article [12], devoted to an investigation of stationary behaviors, we showed that deformations of large amplitude may become unstable above a beam power threshold, leading to the formation of a long-beam centered jet. We also proposed an instability mechanism based on total reflection of light within the induced deformation. From a fundamental point of view, the investigation of the corresponding dynamics would obviously bring new insights into the mechanism of this "optohydrodynamic" instability which illustrates the subtle nonlinear couplings between laser propagation and interface deformation. As the instability leads to the formation of liquid microjets, this is also of practical interest for the development of optically driven applications analogous to electrospraying [16] or ink-jet printing [17].

Our aims are thus the following: (i) to identify the characteristic time scales of the interface motion in the linear regime, (ii) to evidence a slow dynamics just beyond the instability threshold that is characteristic of a subcritical instability, and (iii) to study whether the interface dynamics at instability onset is compatible with our model of total internal reflection induced instability. In Sec. II, we summarize the main results of the preceding companion article [12], which constitute an indispensable background to the present study of the dynamics of interface deformations. Section III is dedicated to a theoretical description of the linear dynamics of the interface when suddenly submitted to the radiation pressure of a Gaussian cw laser beam. In Sec. IV, we present our measurements of the characteristic time scale of the overdamped hump height and curvature dynamics for small-amplitude interface deformations and compare them to the prediction of the linear theory. Finally, in Sec. V we model our measurements of the interface dynamics at instability onset and link them to the model of total internal-reflection-induced instability.

II. OVERVIEW ON STEADY LASER-DRIVEN INTERFACE DISTORTION

Let us assume a liquid interface intercepted by a continuous laser wave propagating vertically along the z axis. The amplitude of the resulting steady distortion of the flat liquid surface induced by the optical radiation pressure depends on the combined effects of gravity and surface tension. Assuming cylindrical coordinates and denoting r the radius, the surface height $h(r)$ is given by [12]

$$(\rho_1 - \rho_2) g h(r) - \frac{\sigma}{r} \frac{\partial}{\partial r} \left(\frac{r h'(r)}{\sqrt{1 + h'(r)^2}} \right) = \Pi(r, \theta_i), \qquad (1)$$

where ρ_1 and ρ_2 are the densities of the two superposed liquids, σ is the surface tension, and $\Pi(r, \theta_i)$ is the optical radiation pressure for an incidence angle θ_i. In the linear regime of deformation, one has $|h'(r)| \ll 1$ and the value of the radiation pressure can be taken at normal incidence ($\theta_i = 0$) [see, for instance, Eq. (9) of Ref. [12]]. Then, for an incident beam in the TEM_{00} mode, the solution for $h(r)$ can be calculated by use of a Fourier-Bessel, or Hankel, transform.

By comparing the relative effects of the hydrostatic pressure (buoyancy) to that of the Laplace pressure (surface ten-

sion), one can define an optical Bond number as $\mathrm{Bo}=(\omega_0/\ell_c)^2$, where ω_0 is the beam waist of the incident beam and $\ell_c=\sqrt{\sigma/g(\rho_1-\rho_2)}$ is the capillary length associated with the interface. When $\mathrm{Bo}\ll 1$, gravity turns out to be negligible for the surface distortion. The height of the deformation is in this case inversely proportional to the surface tension σ and is thus considerably enhanced when σ is small. That is why our experiments are performed in a water-in-oil microemulsion (stable suspension of surfactant-coated water nanodroplets, called micelles, dispersed in an oil-rich continuum). The composition and some of the characteristics of the chosen microemulsion have already been described [12]. For a temperature $T>T_c$, where $T_c=308$ K is the critical temperature, the mixture separates into two micellar phases ϕ_1 and ϕ_2 of different micellar concentrations. As the density (index of refraction) of water is larger (smaller) than that of oil, the micellar phase ϕ_1 with the larger concentration is located below the low-micellar-concentration phase ϕ_2, whereas its refractive index n_1 is smaller than n_2 of ϕ_2. The main advantages of this type of medium are (i) the intrinsically weak surface tension of the liquid meniscus separating the two phases (due to the presence of surfactant molecules), (ii) the ability to even reduce this surface tension by approaching the critical point (surface tension is typically 10^6 times smaller at $T-T_c=3$ K than that of the water-air free surface), and (iii) the universality of the phenomena observed in the vicinity of a critical point, because our mixture belongs to the universality class $(d=3,n=1)$ of Ising model [18].

Low residual optical absorption at the wavelength used is also required to prevent disturbing thermal heating. This last condition is fulfilled for our micellar phases since the optical linear absorption is $\alpha_0=3\times10^{-4}$ cm^{-1} and the propagation distance is of the order of 1 mm. As a consequence, continuous laser waves can easily create interface deformations without inducing thermal coupling or optical bulk nonlinearity. Critical universality also allows us to evaluate the experimental parameters of our system according to the following universal scaling laws for surface tension and the density contrast between the two phases: $\sigma=\sigma_0[(T-T_c)/T_c]^{2\nu}$, with $\nu=0.63$ and $\sigma_0=10^{-4}$ J m^{-2}, and $\Delta\rho=\rho_1-\rho_2=\Delta\rho_0[(T-T_c)/T_c]^{\beta}$, with $\beta=0.325$ and $\Delta\rho_0=284$ kg m^{-3}. Since the two phases ϕ_1 and ϕ_2 are of similar composition, we assumed the Clausius-Mossotti relation $\Delta n\approx(\partial n/\partial\rho)_T\Delta\rho$ to be valid for the refractive-index contrast $\Delta n=n_1-n_2$, with $(\partial n/\partial\rho)_T=-1.22\times10^{-4}$ m^3 kg^{-1}.

The experimental setup is described in Ref. [12]. The mixture is enclosed in a thermoregulated spectroscopic cell, and the temperature is chosen above T_c to reach the two-phase equilibrium state. The bending of the liquid-liquid meniscus is driven by a linearly polarized TEM_{00} cw Ar^+ laser (wavelength in vacuum $\lambda_0=514.5$ nm) propagating either upward or downward along the vertical axis. The beam is focused on the interface by a microscope objective (Leitz; 10×; N.A., 0.25). In what follows, P is the beam power. We adjust the beam waist ω_0 (evaluated at $1/e^2$) by changing the distance between a lens and the focusing objective. The focal length used is $f=0.3$ m (1 m) for the upward (downward) propagating beam. Interface deformations are illuminated by a white light source and observed using a standard or a high-speed charge-coupled-device (CCD) video camera.

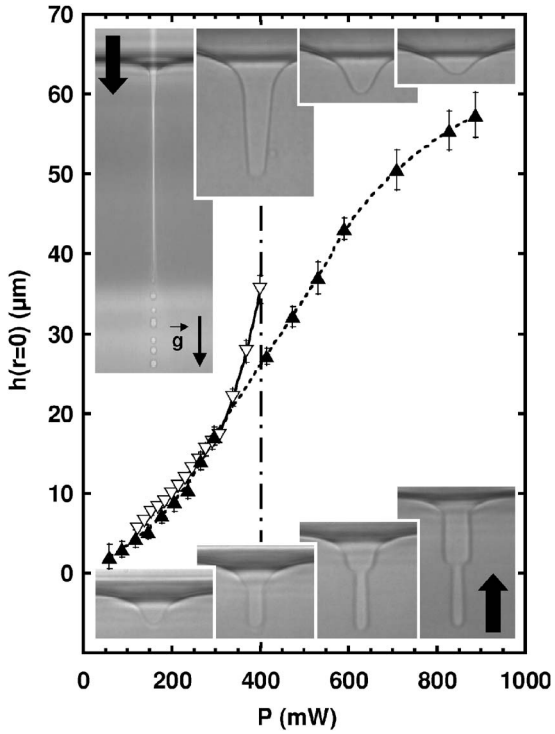

FIG. 1. Variation of the height $h(r=0)$ of the interface deformation versus the incident beam power P when the laser propagates upward (▲) and downward (▽). Lines are just guides for the eye. The bottom set of pictures illustrates the evolution of the deformation for an upward excitation with the emergence of a tetherlike shape; from left to right: $P=270$, 410, 590, and 830 mW. The top set of pictures shows the evolution of the deformation for a downward excitation with the interface disruption and the formation a liquid jet which appear above the threshold power $P_\uparrow$ schematized by the dash-dotted line; from right to left: $P=310$, 370, and $P=P_\uparrow=400$ mW at instability onset and $P=400$ mW at steady state (picture not on scale). $\omega_0=5.3$ μm, $T-T_c=3$ K.

Typical interface deformations induced at $T-T_c=3$ K and $\omega_0=5.3$ μm are presented in Fig. 1 for both upward- and downward-directed beams. As $n_1<n_2$, the radiation pressure acts downward toward the less-refractive medium, regardless of the direction of propagation of the laser [12]. Figure 1 also shows the variation of the height $h(r=0)$ versus beam power P in both cases. As expected and already discussed [12], $h(r=0)$ is proportional to P at low beam power. In the presented example, this regime corresponds to $P\leqslant225$ and 300 mW, respectively, for upward and downward beam excitation. With further increase in P, $h(r=0)$ gradually deviates from linearity. The deformation switches from the classic bell shape to a stable tether shape in the upward-directed case (see the three last pictures at the bottom of Fig. 1). The behavior is radically different for downward excitation. The deformation suddenly loses stability and diverges above a well-defined threshold power $P=P_\uparrow=400$ mW (see the second picture on top of Fig. 1) which corresponds to the instability onset. This instability gives birth to a stationary liquid jet emitting droplets (see the first picture on top of Fig. 1). Guiding of the beam by the jet is also clearly evidenced.

More insights into the underlying physics can be found from the investigation of the interface dynamics leading to these stationary regimes of deformation. This is the purpose of the next section, where the theoretical background required to analyze experimental data is presented.

III. THEORY OF THE INTERFACE LINEAR DYNAMICS

A. Scaling approach

The dynamics of the interface can be first analyzed using a simple scaling approach. Considering the small size of the hump induced by the laser beam of typical waist $\omega_0 \sim 10^{-5}$ m [12], we assume that the characteristic velocity V of the flow associated with the hump formation can be deduced from the creeping flow approximation. Thus, V is set by the balance of the radiation pressure Π and the viscous stresses, which scale as $\eta V/\omega_0$ (η is the dynamic viscosity). Consequently, $V \sim \Pi\omega_0/\eta$ and the characteristic time scale τ of formation of a hump of height h is $\tau \sim h/V$.

Two asymptotic regimes can be analyzed. In the $\mathrm{Bo} \ll 1$ regime, where gravity effects are negligible, $h \sim \Pi\omega_0^2/\sigma$ [12], so $\tau \sim \eta\omega_0/\sigma$. In the $\mathrm{Bo} \gg 1$ regime, where interfacial effects are negligible, $h \sim \Pi/(g\Delta\rho)$ [12], where $\Delta\rho$ is the density contrast between the two liquids, so $\tau \sim \eta/(g\Delta\rho\omega_0)$.

B. Linear one-fluid model

The dynamics of a small amplitude deformation of the free surface of a liquid of density ρ and refractive index n when submitted to the electromagnetic radiation pressure of a laser beam was theoretically described first by Ostrovskaya [19]. This dynamics was analyzed by solving the unsteady, linearized Navier-Stokes and mass conservation equations in cylindrical coordinates with the linearized boundary condition at the free surface detailed in the following. In the unsteady linear model, the small-amplitude deformation hypothesis allows one to linearize the pressure continuity condition at the free surface in the same manner as Eq. (9) of the first companion article [12]:

$$\rho g h(r,t) - \sigma \frac{1}{r}\frac{d}{dr}[r h'(r,t)] - 2\eta \frac{\partial v_z}{\partial z}(r,t) = \Pi(r,t,\theta_i(r,t)=0), \tag{2}$$

where $\eta = \rho\nu$ is the liquid dynamic viscosity, $v_z(r,t)$ is the vertical velocity field of the liquid, and

$$\Pi(r,t,\theta_i(r,t)=0) = \frac{2P}{\pi\omega_0^2 c}\frac{2n(n-1)}{n+1} e^{-r^2/2\omega_0^2} H(t) \tag{3}$$

is the radiation pressure field acting on the free surface at normal incidence. We assume interface excitation by a cylindrical Gaussian beam of waist ω_0 and power P, switched on at time $t=0$ (H is the Heaviside function). This linear set of equations was solved using the Hankel transform $\mathfrak{H}$ with respect to coordinate r, defined as $\mathfrak{H}\{f\}(k) = \int_0^{+\infty} r J_0(kr) f(r) dr$, and the Laplace transform $\mathfrak{L}$ with respect to time, defined as $\mathfrak{L}\{g\}(s) = \int_0^{+\infty} e^{-st} g(t) dt$. The evolution of the surface deformation is finally obtained using the approximation $h(r,t) \simeq \int_0^t v_z(r, z=0, t') dt'$ with

$$v_z(r,z=0,t) = \frac{P}{\pi c \eta}\frac{n(n-1)}{n+1}\int_0^{+\infty} \frac{J_0(kr) e^{-k^2\omega_0^2/8}}{\nu k^2} \times \mathfrak{L}^{-1}\left\{\frac{1}{[A^2(k,s)+1]^2 - 4A(k,s) + \Delta(k)}\right\} dk, \tag{4}$$

where

$$A^2(k,s) = 1 + \frac{s}{\nu k^2}, \tag{5}$$

$$\Delta(k) = \frac{gk + \dfrac{\sigma k^3}{\rho}}{(\nu k^2)^2}. \tag{6}$$

Since $\mathfrak{L}^{-1}\{1/f(s)\}(t) = \Sigma_i e^{s_i t}/f'(s_i)$ when the function $f(s)$ has only simple, isolated poles s_i [20], the time scales of the motion of a deformation characterized by the wave number k are the roots of the denominator of the last term of the integrand in Eq. (4), which is precisely the dispersion relation for plane surface waves of wave number k at a free surface of a viscous liquid [21]. The physically acceptable roots of the dispersion relation have to support $\mathrm{Re}[A^2(k,s)] \geqslant 0$ in order to satisfy the boundary condition $v_z(r,z,t) \xrightarrow[z\to-\infty]{} 0$ [19,22].

C. Characteristic time scales obtained from the dispersion relation

The one-fluid model can be adapted to the interface between two liquids 1 and 2 by applying to Eqs. (4)–(6) the following transformations [23]:

$$\rho \leftrightarrow \rho_1 + \rho_2, gk + \frac{\sigma k^3}{\rho} \leftrightarrow \frac{\rho_1 - \rho_2}{\rho_1 + \rho_2} gk + \frac{\sigma}{\rho_1 + \rho_2} k^3, \eta \leftrightarrow \eta_1 + \eta_2.$$

Thus, a realistic order of magnitude of the characteristic time scales of the evolution of the interface deformations observed in our experiment should be obtained by solving the dispersion relation of interfacial viscous waves of wave number k:

$$\left(s + 2\frac{\eta_1+\eta_2}{\rho_1+\rho_2}k^2\right)^2 + \Omega(k)^2 = 4\left(\frac{\eta_1+\eta_2}{\rho_1+\rho_2}k^2\right)^2 \sqrt{1 + \frac{s}{\dfrac{\eta_1+\eta_2}{\rho_1+\rho_2}k^2}}, \tag{7}$$

$$\Omega(k)^2 = \frac{\rho_1 - \rho_2}{\rho_1 + \rho_2} gk + \frac{\sigma}{\rho_1 + \rho_2} k^3, \tag{8}$$

with

$$\mathrm{Re}\left(1+s\left(\frac{\eta_1+\eta_2}{\rho_1+\rho_2}k^2\right)^{-1}\right)\geqslant 0.$$

As the interface is excited by a laser beam of waist ω_0, we assume the characteristic length scale of interface deformation to be ω_0—i.e., $k\simeq\omega_0^{-1}$.

This dispersion relation is often handled for "low-viscosity" liquids—i.e., for $\Omega(k)\gg[(\eta_1+\eta_2)/(\rho_1+\rho_2)]k^2$—resulting in propagative damped gravitational capillary waves of approximate pulsation $\Omega(k)$ and damping time scale $\{2[(\eta_1+\eta_2)/(\rho_1+\rho_2)]k^2\}^{-1}$ [9,19]. Given the small values of $\omega_0\sim 10^{-5}$ m, of $\sigma\sim 10^{-7}$ J m^{-1}, and of $\rho_1-\rho_2\sim 50$ kg m^{-3} encountered in our experiments and given $\rho_1\simeq\rho_2\sim 1000$ kg m^{-3}, $\eta_1\simeq\eta_2\simeq\langle\eta\rangle\sim 10^{-3}$ kg m^{-1} s^{-1}, we find instead $\Omega(k)\ll[(\eta_1+\eta_2)/(\rho_1+\rho_2)]k^2$. Thus, the interface dynamics falls in the so-called regime of overdamped surface waves [24,25]. In the $\Omega(k)\ll[(\eta_1+\eta_2)/(\rho_1+\rho_2)]k^2$ limit, Eq. (7) has (i) two complex, conjugate roots $s_{1,2}(k)\simeq[(\eta_1+\eta_2)/(\rho_1+\rho_2)]k^2(-1.77\pm 1.11i)$ that are to be rejected since $\mathrm{Re}[A^2(k,s_{1,2})]<0$ and (ii) two real roots $s_3(k)\simeq -0.91[(\eta_1+\eta_2/\rho_1+\rho_2)]k^2$ and $s_4\simeq-\Omega(k)^2\{2[(\eta_1+\eta_2)/(\rho_1+\rho_2)]k^2\}^{-1}$ [21]. Consequently, the interface motion is not oscillatory but just damped. Finally, assuming $k\simeq\omega_0^{-1}$,we find $|s_3|\simeq 10^5$ s^{-1} and $|s_4|\simeq 10^2$ s^{-1}—i.e., $|s_4|\ll|s_3|$ in our experimental conditions. Consequently, the interface motion characterized by s_3, corresponding to the viscous diffusion of momentum over the length scale ω_0, is damped very rapidly, and the interface motion should be mainly damped on the time scale $\tau=-s_4^{-1}$ which can be expressed as

$$\tau(k)=\frac{2(\eta_1+\eta_2)k^2}{(\rho_1+\rho_2)\Omega(k)^2}\simeq\frac{4\langle\eta\rangle}{\sigma k}[1+(k\ell_c)^{-2}]^{-1}. \tag{9}$$

Using $k=\omega_0^{-1}$, τ can be written as

$$\tau(\omega_0^{-1})\simeq\frac{4\langle\eta\rangle\omega_0}{\sigma}(1+\mathrm{Bo})^{-1}, \tag{10}$$

with $(\eta_1+\eta_2)/2\simeq\langle\eta\rangle=1.27\times 10^{-3}$ Pa s [26] and $(\rho_1+\rho_2)/2\simeq\langle\rho\rangle=871.6$ kg m^{-3}. The dispersion relation of the plane interfacial waves predicts that the characteristic time scale of the hump relaxation should scale as $\tau(\omega_0^{-1})=\tau_0=4\langle\eta\rangle\omega_0/\sigma$ in the $\mathrm{Bo}\ll 1$ regime and as $\tau(\omega_0^{-1})=\tau_\infty=4\langle\eta\rangle/g\omega_0\Delta\rho$ in the $\mathrm{Bo}\gg 1$ regime, as suggested by the scaling approach.

D. Overdamped dynamics of the hump height and curvature

As we measured the dynamics of both the hump height $h(0,t)$ and the hump curvature,

$$\kappa(0,t)=\frac{1}{r}\frac{d}{dr}\left(r\frac{dh}{dr}\right)(0,t)$$

in the $\mathrm{Bo}\ll 1$ and $\mathrm{Bo}\simeq 1$ regimes, here we study numerically the actual behavior of these quantities with respect to the Bo number. The major concern of this section is to determine whether the prediction, Eq. (10), for the characteristic time scale of evolution of both the hump height and curvature obtained from the dispersion relation of plane interfacial waves is realistic in the case of an axisymmetric deformation induced by a Gaussian laser beam.

Using the physically acceptable roots of the dispersion relation presented in the last section and neglecting the rapidly damped motion characterized by s_3, we can transform and integrate Eq. (4) to get

$$h(0,t)\simeq-\frac{\Pi_0\omega_0^2}{2(\rho_1+\rho_2)}\int_0^\infty\frac{k^2}{\Omega(k)^2}e^{-k^2\omega_0^2/8}(1-e^{s_4(k)t})dk \tag{11}$$

and

$$\kappa(0,t)\simeq-\frac{\Pi_0\omega_0^2}{2(\rho_1+\rho_2)}\int_0^\infty\frac{k^4}{\Omega(k)^2}e^{-k^2\omega_0^2/8}(1-e^{s_4(k)t})dk, \tag{12}$$

after a time long compared to $|s_3|^{-1}$. Here

$$\Pi_0=\frac{4Pn_i}{\pi c}\frac{n_2-n_1}{\omega_0^2 n_2+n_1}$$

is the radiation pressure along the beam axis [12], where the index i refers to the incident fluid. The integrals appearing in Eqs. (11) and (12) are first made dimensionless:

$$h(0,t)=\frac{\Pi_0\omega_0^2}{2\sigma}\int_0^\infty e^{-x^2/8}\frac{1}{1+\dfrac{\mathrm{Bo}}{x^2}}\left[1-\exp\left(-t^*x\frac{1+\dfrac{\mathrm{Bo}}{x^2}}{1+\mathrm{Bo}}\right)\right]\frac{dx}{x}, \tag{13}$$

$$\kappa(0,t)=-\frac{\Pi_0}{2\sigma}\int_0^\infty e^{-x^2/8}\frac{1}{1+\dfrac{\mathrm{Bo}}{x^2}}\left[1-\exp\left(-t^*x\frac{1+\dfrac{\mathrm{Bo}}{x^2}}{1+\mathrm{Bo}}\right)\right]xdx, \tag{14}$$

where $t^*=t/\tau(\omega_0^{-1})$ and $x=k\omega_0$, then computed numerically using MATLAB.

In order to compare the time evolutions of $h(0,t)$ and $\kappa(0,t)$ computed at various values of Bo and when such an approximation was found to be acceptable, we chose to fit the reduced hump height $h^*(t)=h(0,t)/h(0,t_{\max})$ and the reduced curvature $\kappa^*(t)=\kappa(0,t)/\kappa(0,t_{\max})$ over the time interval $[0,t_{\max}]$ with the experimentalist-friendly function $1-e^{-t/\tau_{\mathrm{eff}}}$, τ_{eff} being the only free parameter of the fit.

1. Hump height behavior

The variations of h^* versus the reduced time t^* are plotted in Fig. 2 for several values of Bo, together with their best exponential fit computed on the range $[0,t_{\max}=100\tau(\omega_0^{-1})]$. $h^*(t^*)$ is found to relax monotonously up to unity, qualitatively as its exponential fit. But $h^*(t^*)$ is satisfactorily fitted by an exponential only for $\mathrm{Bo}\geqslant 10^{-2}$. In this range, $\tau_{\mathrm{eff}}/\tau(\omega_0^{-1})$ varies between 2.35 and 0.8 (some values are given in the caption of Fig. 2). This means that in the Bo

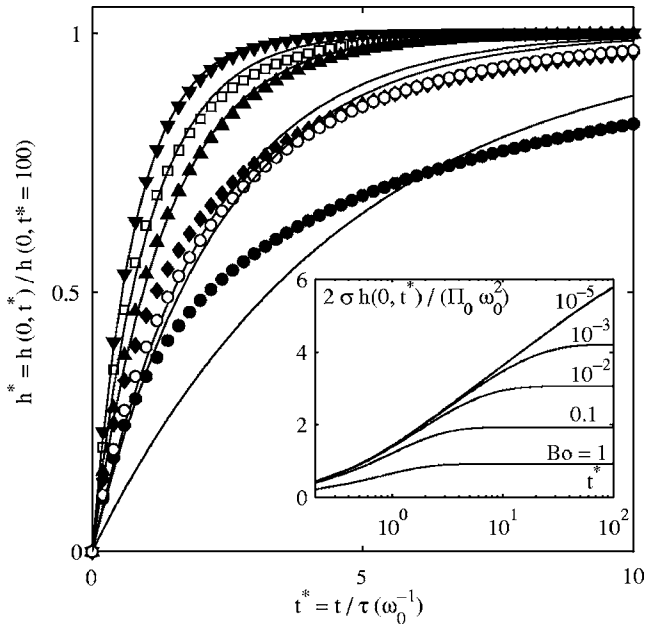

FIG. 2. Variations of the reduced hump height $h^*(t)=h(0,t)/h(0,100\tau(\omega_0^{-1}))$ as a function of the reduced time $t^*=t/\tau(\omega_0^{-1})$ [defined by Eq. (10)] for several Bo values. Solid lines are best exponential fits $1-e^{-t/\tau_{\text{eff}}}$ to $h^*(t)$. $\tau_{\text{eff}}/\tau(\omega_0^{-1})=$(●) 4.73 (Bo=$10^{-3}$), (♦) 2.15 (Bo=$10^{-2}$), (□) 1.06 (Bo=0.1), (▼) 0.8 (Bo=1), (▲) 1.36 (Bo=10), and (○) 2.35 (Bo∞). Inset: time evolution of the dimensionless hump height $2\sigma h(0,t^*)/\Pi_0\omega_0^2$, defined by Eq. (13), shown in log-linear scales, for several values of Bo.

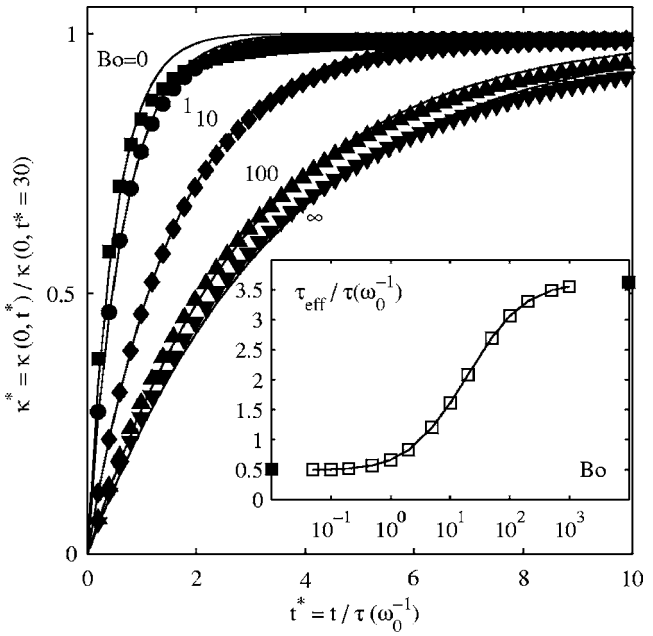

FIG. 3. Variations of the reduced hump curvature $\kappa^*(t^*)=\kappa(0,t^*)/\kappa(0,30)$ as a function of the reduced time $t^*=t/\tau(\omega_0^{-1})$ [defined by Eq. (10)] for several Bo values indicated nearby them. Solid lines are best exponential fits $1-e^{-t/\tau_{\text{eff}}}$ to $\kappa^*(t)$. Inset: (□) variation of the reduced characteristic time scale of evolution of $\kappa^*(t)$, $\tau_{\text{eff}}/\tau(\omega_0^{-1})$, versus Bo. (■) Asymtotic values of $\tau_{\text{eff}}/\tau(\omega_0^{-1})$ for Bo$\to$0 and ∞.

$\geqslant 10^{-2}$ regime, the prediction of the dispersion relation of interfacial plane waves is realistic.

On the contrary, for Bo$<10^{-2}$, $h^*(t^*)$ relaxes rapidly, then very slowly up to unity, and it is not satisfactorily fitted by an exponential. As a matter of fact, the relaxation presents a logarithmic behavior which is more pronounced as Bo decreases. The time evolution of the dimensionless height $2\sigma h(0,t^*)/\Pi_0\omega_0^2$ defined by Eq. (13) is shown in log-linear scales in the inset of Fig. 2. A late-stage linear behavior is indeed observed, which is longer as Bo decreases. This late-stage logarithmic evolution of $h(0,t)$ is linked to the fact that the static hump height diverges as ln(Bo) as Bo tends to zero (by making $g=0$ or $\omega_0=0$) [12,28]; see Eq. (17) in Ref. [12]. Consequently, the temporal behavior of the hump height at very small Bo number is more complex than predicted by the dispersion relation of plane interfacial waves.

2. Hump curvature behavior

We first consider the behavior of κ^* versus t^* without gravity (Bo=0), presented in Fig. 3 together with its best exponential fit computed on the range $[0,t_{\max}=30\tau(\omega_0^{-1})]$. As shown in Ref. [10],

$$\kappa^*(t^*) \propto t^* e^{2t^{*2}} \text{erfc}(\sqrt{2}t^*). \tag{15}$$

Its best exponential fit gives $\tau_{\text{eff}}\simeq 0.48\tau_0$. This means that in the Bo$\ll 1$ regime and concerning the dynamics of the hump curvature, the prediction of the dispersion relation of interfacial plane waves is realistic. Furthermore, the effective wave number to be used in the dispersion relation is $k_{\text{eff}}\simeq 2.1\omega_0^{-1}$.

We now consider the behavior of $\kappa^*(t^*)$ without surface tension (Bo=∞), shown in Fig. 3. Its best exponential fit gives $\tau_{\text{eff}}\simeq 3.62\tau_\infty$. This means that in the Bo$\gg 1$ regime, the prediction of the dispersion relation of interfacial plane waves is also realistic. In this case, the effective wave number to be used in the dispersion relation is $k_{\text{eff}}\simeq 3.6\omega_0^{-1}$.

We finally consider the variations of $\kappa^*(t^*)$, plotted in Fig. 3 for several values of Bo, together with their best exponential fit. The agreement between $\kappa^*(t^*)$ and its best exponential fit is found to be very satisfactory at any Bo value. The variation of the reduced characteristic time scale of relaxation of $\kappa^*(t^*)$, $\tau_{\text{eff}}/\tau(\omega_0^{-1})$ versus Bo is shown in the inset of Fig. 3. The observed weak variation of $\tau_{\text{eff}}/\tau(\omega_0^{-1})$ over the wide range Bo$=5\times 10^{-2}$—10^3 shows that τ_{eff} actually scales as $\tau(\omega_0^{-1})$ both in the Bo$\ll 1$ and Bo$\gg 1$ regimes. Thus, the use of $k=\omega_0^{-1}$ in the dispersion relation of plane interfacial waves gives the right order of magnitude for the characteristic time scale of evolution, τ_{eff}, of the hump curvature $\kappa(0,t)$ at any Bo value. In particular, $\tau_{\text{eff}}\simeq 0.5\tau(\omega_0^{-1})$ holds up to Bo$\simeq 1$.

To summarize this section, the numerical study demonstrates that (i) the behavior of the hump curvature evolution $\kappa(0,t)$ is close to an exponential relaxation at any Bo value, (ii) it is also the case for the hump height evolution $h(0,t)$ in the range Bo$>10^{-2}$, (iii) in these ranges of Bo, the characteristic time scales of evolution of the hump height and curvature are correctly predicted by the dispersion relation of plane interfacial waves assuming $k=\omega_0^{-1}$, and (iv) in the range Bo$<10^{-2}$, the hump height evolution shows up a no-

ticeable late-stage logarithmic evolution that makes simple exponential fits irrelevant.

IV. MEASUREMENT OF THE CHARACTERISTIC TIME SCALE OF THE INTERFACE MOTION

In order to experimentally characterize the time scale of the interface deformation dynamics when it is submitted to the radiation pressure of a laser beam, we proceeded in two ways. At first, we captured the motion of the hump formed at the interface, extracting its height $h(0,t)$ along the beam axis. Then, we used the focusing property of the interface hump [4] in the same way as Sakai *et al.* [27] to measure the dynamics of the hump curvature along the beam axis $\kappa(0,t)$. We present sequentially our measurements of both the hump height and curvature dynamics, and compare them to their prediction presented above.

A. Hump height dynamics

The experimental setup is described in detail in the preceding companion article [12]. We captured the motion of the interface using a high-speed motion meter Redlake digital video camera of resolution 292×220 acquiring 250 fps. Then we extracted the hump height along the beam axis $h(0,t)$ from the pictures. We performed these experiments in the temperature range $T-T_C=5-25$ K and for a beam waist varying from 5 to 8.9 μm, corresponding to a range of Bo number $7\times10^{-3}-0.1$. A typical evolution of the interface distortion against time is shown in Fig. 4.

A series of hump height evolutions is shown in the inset of Fig. 5. In order to be allowed to compare our measurements of τ_{eff} to the linear model presented in Sec. III D 1, experiments have to be performed in the linear regime; i.e., the measured value of τ_{eff} has to be independent of the beam power P. To check this requirement and simultaneously measure τ_{eff}, we used the procedure illustrated in Fig. 5 for each chosen couple $(\omega_0, T-T_c)$. The temporal behavior of $h(0,t)$ is extracted from the image analysis for several beam power values. Then, as explained in Sec. III, the curves are independently fitted with an exponential function in order to get both the asymptotic hump height $h(0,\infty)$ and the relaxation time scale τ_{eff}, as illustrated in the inset of Fig. 5. The deduced asymptotic hump heights are used to reduce the height $h(0,t)$. An example of data reduction, expected for the linear regime of deformation, is presented in Fig. 5. On the other hand, the measurement of different values of the relaxation time allows the determination of a mean value of τ_{eff}, which must be retrieved from the fit of the full reduced data set.

Since the experiments were performed in the range of Bo number, $7\times10^{-3}-0.1$, an exponential fit of $h(0,t)$ is relevant, as shown by the numerical study presented in Sec. III D 1, and the effective time scale of exponential relaxation of the hump height, τ_{eff}, should scale as $\tau_0=4\langle\eta\rangle\omega_0/\sigma$. Thus, τ_{eff} should increase versus both the beam waist and the vicinity to the critical point. The first expectation is confirmed in Fig. 6, while an example of the second one is given in the inset.

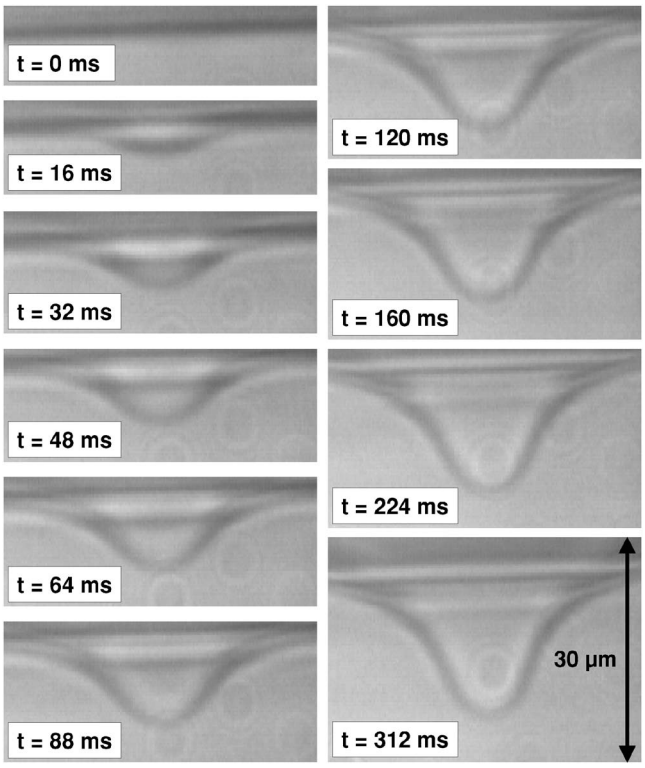

FIG. 4. Typical temporal behavior of an interface distortion in the regime of linear deformation when the cw optical excitation is suddenly applied at time $t=0$ s. The parameters are $P=840$ mW, $\omega_0=6.3$ μm, and $T-T_c=10$ K.

Finally, the variation of τ_{eff} versus τ_0, plotted in Fig. 7 in log-log scales, is compatible with the predicted scaling law, despite a large experimental scatter. In particular, the slope of the best linear fit of the experimental data, 1.88, is located between the value of $\tau_{\text{eff}}/\tau(\omega_0^{-1})$ at Bo$=10^{-2}$: namely, 2.15 and its value at Bo$=10^{-1}$, 1.06.

Nevertheless, we must note that this method suffers from a major drawback. Since we use near-critical interfaces, the refractive index contrast between the two phases at coexistence is intrinsically weak. Interfaces are thick and weakly contrasted, making the detection of interface profiles difficult. This drawback is enhanced by the fact that we must use a long-working-distance microscope objective to observe the interface, due to the presence of an oven around the cell containing the sample. Consequently, the resulting depth of field is quite large, reducing the optical resolution. This and the usual sensitivity of near-critical fluids properties to any thermal and composition gradients probably explain the scattering of the data.

B. Hump curvature dynamics

In order to get more reliable results, we extended to liquid-liquid interfaces a method used to quantitatively characterize laser beam self-focusing in nonlinear media [29] and, more recently, to measure surface tension at liquid free surfaces [27].

The experimental setup used to measure the dynamics of the interface hump curvature is shown in Fig. 8. It consists in

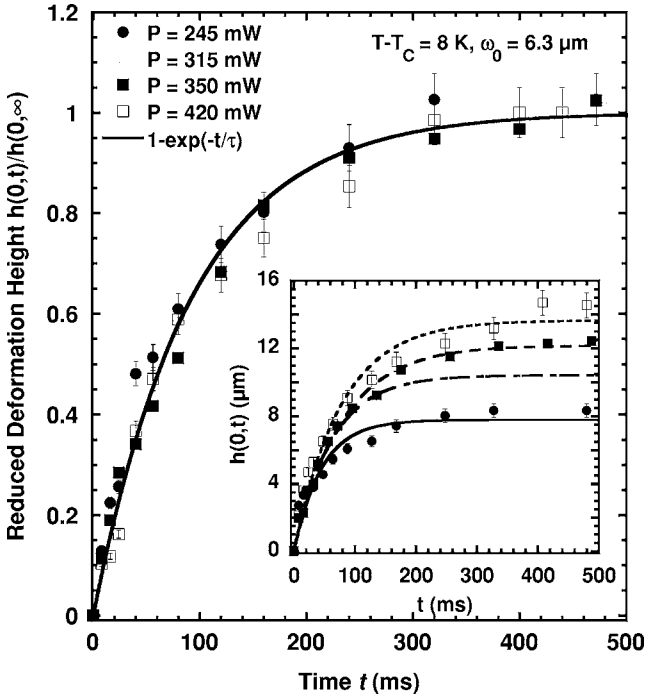

FIG. 5. Temporal evolution of the reduced hump height $h(0,t)/h(0,\infty)$ corresponding to the temporal evolutions of the hump height observed for various beam powers shown in the inset. The asymptotic value $h(0,\infty)$ is determined for each P from an exponential fit of $h(0,t)$ shown in the inset.

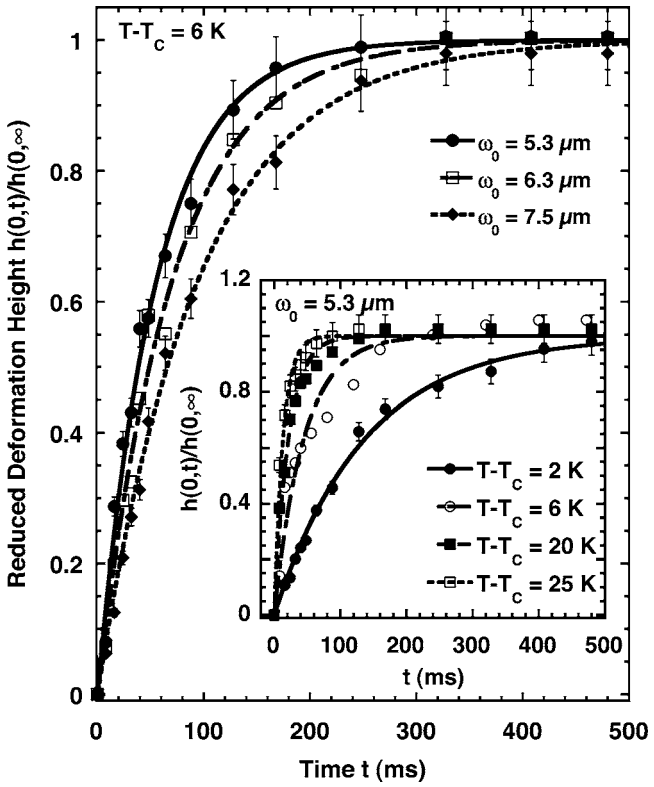

FIG. 6. Temporal behavior of the reduced hump height $h(0,t)/h(0,\infty)$ versus the beam waist ω_0 and the vicinity to the critical point $T-T_c$ (inset). Lines are exponential fits.

measuring the power of the laser beam refracted by the liquid interface and transmitted through a diaphragm of diameter smaller than that of the beam. The laser beam is mechanically chopped with a period of 4 s in such a manner that the illumination of the sample is steady after a very short transient of 4 μs. The time-dependent, bell-shaped deformation induced at the interface by this upward incident beam acts as a convergent lens that focuses the beam. The focused beam emerging from the sample cell is filtered spatially using an iris diaphragm placed between the sample cell and the focus of the refracted beam. The power of this filtered beam is measured as a function of time using a photon counter and a SR430 multichannel analyzer. Thus, the characteristic time scales of the dynamics of the measured optical power are similar to those of the interface deformation dynamics. For interface deformations of curvature small enough so that the resulting focal length of the liquid lens is large compared to the path of the focused beam, the power of the filtered beam is actually proportional to the hump curvature, as shown in the Appendix.

We measured the power detected by the photon counter versus time during the deformation of the interface in the temperature range $T-T_c=2-20$ K and in the range of beam waist, 3.47–31.2 μm, corresponding to a range of Bo number, $10^{-2}-1.8$. A typical temporal evolution of the filtered beam power is shown in the inset of Fig. 9. For interface deformations of small amplitude, the power signal exhibits a monotonous, relaxation behavior from an initial value at the beginning of the irradiation, corresponding to the flat interface, to an asymptotic value, corresponding to the steady, bell-shaped interface acting as a lens. This confirms that the dynamics of the interface deformation is always overdamped, as predicted in Sec. III for the present experimental conditions. This relaxation behavior is also satisfactorily described using a single-exponential relaxation of characteristic time τ_{eff}, as shown in the inset of Fig. 9. As for the measurements of the hump height dynamics, for each measurement of τ_{eff} we checked its independence with respect to the beam power by varying P over a chosen range.

Since the scaling law $\tau_{\text{eff}} \simeq 0.5\tau(\omega_0^{-1})$ was theoretically shown to hold up to $\text{Bo} \simeq 1$ in the case of the hump curvature dynamics, we plotted in Fig. 9 the variation versus $\tau(\omega_0^{-1})$ of the characteristic time scale of the evolution of the hump curvature τ_{eff}, measured for the whole range of Bo, together with its best linear fit of slope 0.98. This value is 2 times larger than its prediction at small Bo number, but close to its predicted value at Bo=2, the upper limit of the investigated range: namely, 0.83 (see Fig. 9). This discrepancy could be attributed to the uncertainty on the value of $\langle \eta \rangle$. Despite this slight discrepancy, we can say that in the $\text{Bo} \ll 1$ and $\text{Bo} \simeq 1$ regimes, the characteristic time scale of the dynamics of the hump curvature obeys the linear model of overdamped relaxation developed in Sec. III.

To summarize this section, we showed theoretically that, given the conditions of our experiment, the dynamics of the interface deformation induced by the electromagnetic radiation pressure is overdamped; i.e., it has a relaxation behavior of characteristic time scale τ_{eff} of the order of a few tens of milliseconds. We showed numerically that, using $k=\omega_0^{-1}$ as

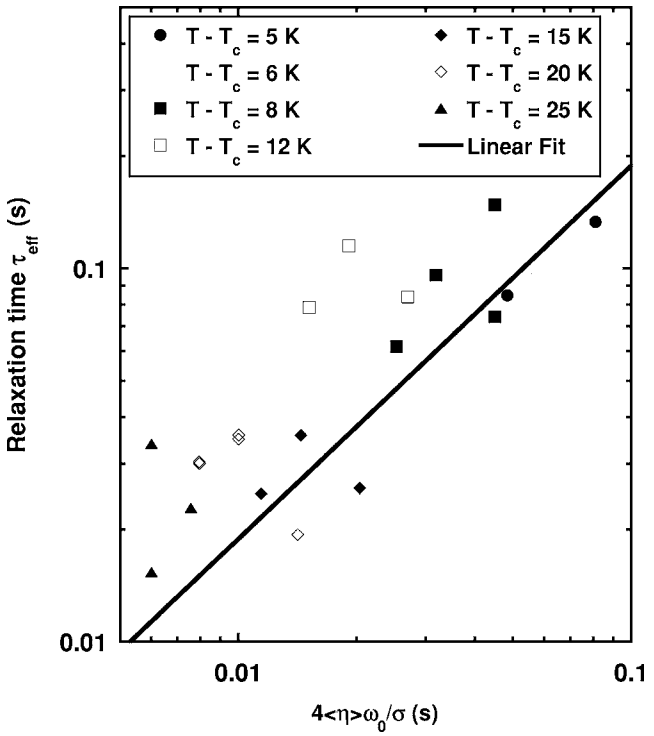

FIG. 7. Variation of the characteristic time scale τ_{eff} of the hump height evolution versus its predicted scaling behavior $4\langle\eta\rangle\omega_0/\sigma$ for several temperatures. The solid line is the best linear fit of slope 1.88.

effective wave number, the linear dispersion relation of plane interfacial waves, Eq. (7), satisfactorily describes the relaxation dynamics of the hump curvature at any Bo value, whereas a noticeable logarithmic divergence characterizes the late-stage evolution of the hump height for $\text{Bo}<10^{-2}$. Finally, we showed experimentally that the characteristic time scale τ_{eff} of the hump height (the hump curvature) relaxation dynamics scales as the theoretically predicted time scale $\tau(\omega_0^{-1})$ in the Bo range $7\times10^{-3}-10^{-1}$ ($10^{-2}-1.8$).

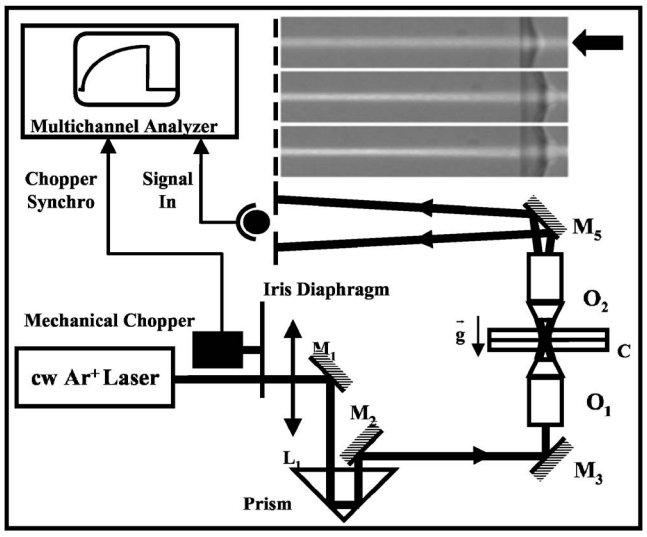

FIG. 8. Experimental setup used to measure the dynamics of the interface hump curvature along the beam axis. The pictures illustrate the beam focusing induced by the interface deformation for increasing beam powers (up to down).

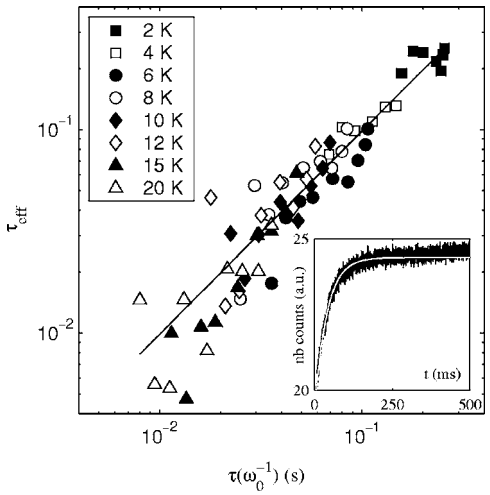

FIG. 9. Variation of the characteristic time scale τ_{eff} of the hump curvature evolution versus its predicted scaling behavior $\tau(\omega_0^{-1})=4\langle\eta\rangle\omega_0/\sigma$. The solid line is the best linear fit of slope 0.98. The Bo number ranges from 10^{-2} to 1.8. Inset: typical power signal measured by the photon counter. The sample temperature is such that $T-T_c=15$ K. The illumination by the laser beam of waist $\omega_0=24.5$ μm and power 500 mW begins at $t=0$. The solid line corresponds to the best fit by an exponential function of characteristic time $\tau_{\text{eff}}=39$ ms.

V. INTERFACE DYNAMICS AT THE ONSET OF THE OPTOHYDRODYNAMIC INSTABILITY

In Ref. [30] and in the preceding companion article [12], we showed that above a given beam power threshold $P_\uparrow$, the interface becomes unstable and forms a long cylinder of very large aspect ratio [31], emitting drops, called hereafter a jet. In order to enlighten the mechanism of the instability leading to the lengthening of the hump and to the formation of the jet, we now study the dynamics of the interface at instability onset.

A. Experimental procedure

To study the influence of the control parameter P of the interface instability on its dynamics just beyond the threshold, we captured the motion of the unstable interface using the high-speed video camera acquiring at a rate of 250 fps. A typical series of pictures of the moving interface above instability threshold is shown in Fig. 10. The interface dynamics was analyzed as a function of both temperature, in the range $T-T_c=2-10$ K, and laser beam power for a fixed beam waist $\omega_0=3.74$ μm, so that the dimensionless distance to the threshold $\Delta P^*=(P-P_\uparrow)/P_\uparrow$ was varied in the range 0–1.6. Once the temperature and beam power are chosen, the experiment proceeds as follows. At $t=0$, the beam shutter is set off, the laser beam suddenly impinges on the interface with a power larger than $P_\uparrow$ and the interface motion is captured up to the exit of the interface tip from the camera field. We stress the fact that, because of experimental constraints,

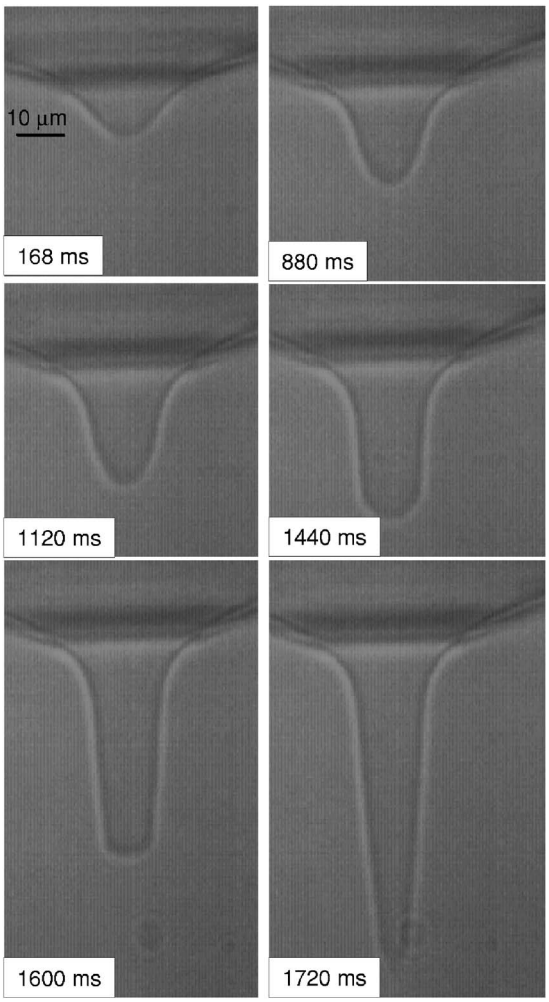

FIG. 10. Sequential pictures of the moving interface at $T-T_c=8$ K above the instability threshold $P_\uparrow=755$ mW. The laser illumination of power $P=840$ mW and waist $\omega_0=3.74$ μm started at $t=0$.

this procedure differs from classical experiments dedicated to the slow dynamics of instabilities at their onset (see, e.g., Ref. [32]), for which the control parameter is suddenly increased from a value just below the instability threshold to a slightly unstable value.

B. Slowing down near the instability threshold

1. Hump height dynamics

In Fig. 11(a) the temporal evolutions of the hump height $h(0,t)$ at $T-T_c=8$ K are plotted for several values of beam power P, the smallest one below threshold $P_\uparrow=760$ mW ($\Delta P^*<0$), the larger ones above it ($\Delta P^*>0$). For $\Delta P^*<0$, $h(0,t)$ shows up a relaxation behavior of characteristic time scale τ_{eff}, similar to the linear dynamics studied in Sec. IV. On the other hand, for $\Delta P^*>0$ each $h(0,t)$ curve exhibits an inflection point at a hump height h_i, which slightly increases with P, and at a time t_i, called hereafter the inflection time, which decreases when P increases. The instability first becomes evident at the inflecion of $h(0,t)$, although it may have begun earlier. The variations of the inflection time t_i

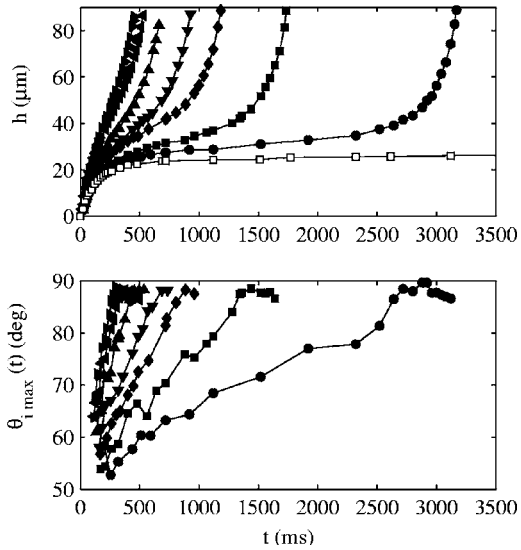

FIG. 11. (a) Temporal evolutions of the interface hump height $h(0,t)$ at $T-T_c=8$ K for several values of beam power P below and above threshold $P_\uparrow=760$ mW: (□) $P=700$ mW. (●) $P=770$ mW. (■) $P=840$ mW. (♦) $P=910$ mW. (▼) $P=980$ mW. (▲) $P=1120$ mW. (◀) $P=1260$ mW. (▶) $P=1400$ mW. (b) Corresponding temporal evolutions of maximum angle of incidence $\theta_{i\,\max}(t)$ along the interface. Symbols are the same.

normalized by τ_{eff} versus ΔP^* are plotted in Fig. 12 in logarithmic scales for several values of $T-T_c$. These variations range over more than a decade and are compatible with a power-law behavior with exponents close to −0.65.

2. Model of subcritical instability

In order to justify our choice of the model describing the dynamics of the hump at the instability onset, we first briefly characterize the stability of the hump and the associated bi-

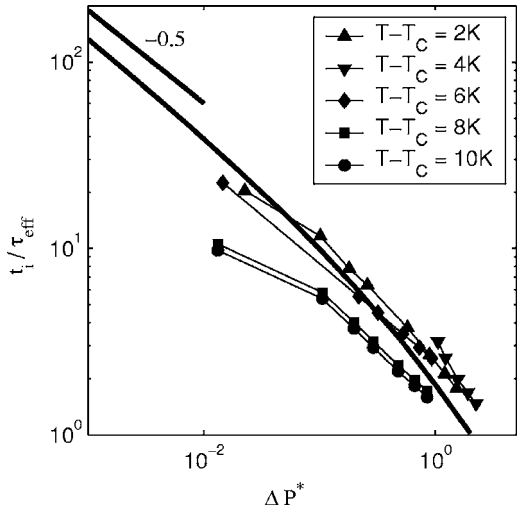

FIG. 12. Instant t_i of inflection of $h(0,t)$ [see Fig. 11(a)] normalized by the characteristic time scale of the relation τ_{eff} below the instability threshold, as a function of the reduced distance to the beam power threshold $\Delta P^*=(P-P_\uparrow)/P_\uparrow$ for several values of $T-T_c$. The solid line is the prediction of a model of imperfect subcritical instability (see Fig. 14).

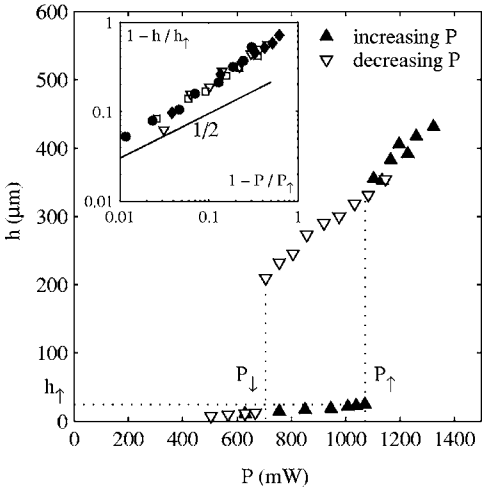

FIG. 13. Hysteresis of the deformation height versus the beam power. $T-T_c=18$ K and $\omega_0=3.5$ μm. The lower branch of the hysteresis corresponds to the static hump studied in Ref. [12], whereas its upper branch corresponds to an elongated shape emitting droplets (jet). Inset: variations of the reduced hump height $1-h/h_\uparrow$ ($h_\uparrow$ is the static hump height at the instability threshold) versus the reduced distance to the threshold $1-P/P_\uparrow$ for several experimental conditions: (□) $T-T_c=4$ K, $\omega_0=3.47$ μm, (♦) $T-T_c=6$ K, $\omega_0=3.47$ μm, (▽) $T-T_c=14$ K, $\omega_0=3.47$ μm, and (●) $T-T_c=4$ K, $\omega_0=3.91$ μm. The solid line is a square root law.

furcation diagram. A more detailed presentation of the experimental results relative to the bifurcation diagram will be the subject of a future article. As shown in Fig. 13, the hump-jet transition is hysteretic; i.e., after its formation at $P\geqslant P_\uparrow$, the jet persists when P is decreased until a second threshold $P_\downarrow<P_\uparrow$. Moreover, the variation of the hump height h versus P close to the instability threshold is characteristic of a saddle-node bifurcation. As shown in the inset of Fig. 13, the variations of the reduced hump height $1-h/h_\uparrow$ [$h=h(0,\infty)$, and $h_\uparrow$ is the static hump height at the threshold; see Fig. 13] versus the distance to the instability threshold $1-P/P_\uparrow$ are indeed compatible with a square root dependence $1-h/h_\uparrow \propto (1-P/P_\uparrow)^{1/2}$ for $1-P/P_\uparrow<10^{-1}$ [33].

These observations, as well as a former analysis of the bistable shape of ferrofluid drops under magnetic field [32], lead to suppose by analogy that at $P=P_\uparrow$ the hump becomes unstable and turns to a more elongated shape, the jet. At this power threshold, the sum of the electromagnetic energy and of the interfacial energy associated to the hump shape is no longer a minimum, but becomes a maximum. Thus, the stability diagram of the hump in the (h,P) plane should predict (i) the linear increase of h with P at small beam powers (static linear regime), (ii) a relaxation dynamics below the threshold of instability, (iii) a saddle-node bifurcation, and (iv) the coexistence of two static equilibrium shapes for the hump in a given range of power below $P_\uparrow$: namely, the small hump and the jet. The stability diagram associated with the first-order, nonlinear equation

$$\frac{d\tilde{h}}{d\tilde{t}}=\tilde{P}-\tilde{h}+b\tilde{h}^2-c\tilde{h}^3, \tag{16}$$

with $\sqrt{3c}<b<\sqrt{4c}$, qualitatively fulfills the above listed requirements. Equation (16) involves dimensionless variables,

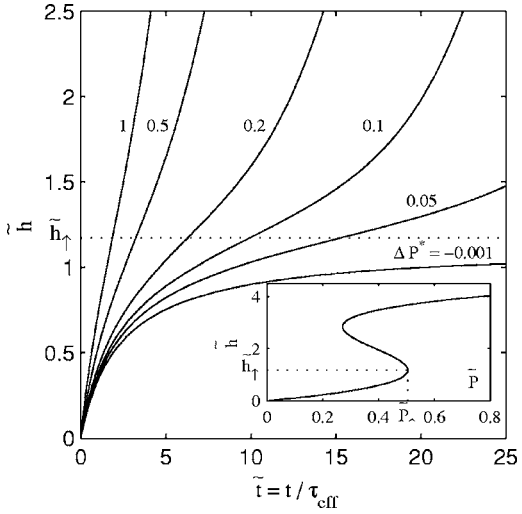

FIG. 14. Temporal evolutions of the reduced height $\tilde{h}(\tilde{t})$ ($\tilde{t}=t/\tau_{\rm eff}$) computed for several distances to the instability threshold ΔP^* using the amplitude equation (16). $\tau_{\rm eff}$ is the characteristic time scale of the hump linear dynamics. inset: stability diagram associated with Eq. (16).

among them a time normalized with the time scale $\tau_{\rm eff}$ of the linear dynamics—i.e., $h(\tilde{t})=h(0,t/\tau_{\rm eff})$. It is similar to the hysteretic magnetization diagram of a single domain under an applied static magnetic field (imperfect subcritical instability [33]). The stability diagram associated with Eq. (16) with $c=0.1$ and $b=0.6$ is shown in the inset of Fig. 14. The hump becomes unstable at $(\tilde{h}_\uparrow,\tilde{P}_\uparrow)$, and the associated bifurcation is a saddle node. Note that close to $\tilde{P}_\uparrow$, $\tilde{h}$ strongly increases, as experimentally observed in Fig. 1.

We now aim to check if Eq. (16) qualitatively reproduces the observed hump height dynamics shown in Fig. 11(a). To agree with the experimental conditions presented in Sec. V A, we computed the solutions of Eq. (16) with $\tilde{h}(0)=0$ as a function of the initial value of the static beam power P. They are plotted in Fig. 14. A relaxation of $\tilde{h}(\tilde{t})$ is observed for $\Delta P^*<0$, while a divergent behavior very similar to Fig. 11(a) is observed for $\Delta P^*>0$ [at longer times, $\tilde{h}(\tilde{t})$ converges to the upper stable branch of the stability diagram shown in the inset of Fig. 14]. Finally, the variation versus ΔP^* of the computed normalized inflection time $t_i/\tau_{\rm eff}$ is compared to the experimental one in Fig. 12. Excellent agreement is found, which confirms the validity over a large range in P of the phenomenological, simple nonlinear model for this instability represented by Eq. (16).

Very close to the instability threshold, the exponent of the effective power law representing the variation of $t_i/\tau_{\rm eff}$ versus ΔP^* computed using Eq. (16) drops to −0.5, as shown in Fig. 12. This value is identical to the analytical prediction and its experimental verification by Bacri and Salin [32] of the time scale of divergence for the eccentricity of ferrofluid drops under a magnetic field above the instability threshold, when the magnetic field is first established at a value slightly lower than the threshold (initially motionless interface). As a matter of fact, in the present experiment, for $0<\Delta P^*\ll 1$, the hump is almost motionless when the instability sets on.

The main difference between this model and measurements is that inflection is experimentally found to occur at a hump height h_i that slightly depends on ΔP^*, whereas the first-order differential equation (16) imposes the condition that inflection ($d^2\tilde{h}/d\tilde{t}^2=0$) occur at $\tilde{h}_\uparrow$, which has no ΔP^* dependance. This discrepancy can probably be ascribed to the fact that the actual interface dynamics is not simply of first order in time, but of overdamped second order.

C. Maximum angle of incidence at inflection of $h(0,t)$

In Ref. [30], we proposed an instability mechanism based on the hypothesis that the instability occurs when the maximum of the angle of incidence along the deformed interface, $\theta_{i\,\max}$, reaches the angle of total reflection θ_{RT}. This leads to the reflection of the whole incident electromagnetic energy towards the tip of the deformation and consequently to a huge increase of the radiation pressure acting on it. We showed in [12] that the instability mechanism should be more complex than expected, since at the instability onset the actual value of $\theta_{i\,\max}$ is smaller than θ_{RT}. In this section, we test whether the interface dynamics at onset is compatible, at least qualitatively, with the proposed model of instability.

We analyzed the unsteady interface shapes with the same technique as for steady ones in the preceding companion article (see Sec. IV D of Ref. [12]). We determined the maximum value of the angle of incidence along the interface $\theta_{i\,\max}$ as a function of time for several temperatures in the range $T-T_c=2-10$ K and several values of power P at a fixed waist $\omega_0=3.74$ μm. The $\theta_{i\,\max}(t)$ curves obtained for several values of P above the threshold $P_\uparrow$ ($\Delta P^*>0$) at $T-T_c=8$ K are plotted in Fig. 11(b). $\theta_{i\,\max}(t)$ is found to be a monotonous function of t up to its maximum 90°. From these data, we plotted in Fig. 15 the value of $\theta_{i\,\max}$ at time t_i of inflection of $h(0,t)$ as a function of ΔP^* for several values of $T-T_c$, together with the corresponding values of θ_{RT}. $\theta_{i\,\max}(t_i)$ is found to increase with ΔP^* from roughly 70° at $\Delta P^*\simeq 0$ up to values roughly equal to θ_{RT} (and undoubtedly smaller than 90°) at large values of ΔP^*. Note that 70° coincides with the value of $\theta_{i\,\max}$ along static interfaces just below the instability threshold (see Sec. IV D of Ref. [12]). Consequently, there is no singular change of the shape of the interface when the instability threshold is reached.

Interpreting the increase of $\theta_{i\,\max}(t_i)$ with ΔP^* in the frame of the reflection-induced instability model and considering Fig. 7 of the preceding companion article [12], we note that the instantaneous amount of incident light that is reflected towards the interface tip at time t_i increases strongly with ΔP^*. If the light that is partially reflected toward the interface tip is actually involved in the instability mechanism, the larger $\theta_{i\,\max}(t_i)$, the faster the instability should grow. Thus, the increase of $\theta_{i\,\max}(t_i)$ with ΔP^*, observed in Fig. 15, is compatible with the observed increase of the growth rate of the instability with ΔP^*, observed in Fig. 11(a).

Finally, the fact that the maximum of $\theta_{i\,\max}(t_i)$ is found in Fig. 15 to be roughly equal to θ_{RT} can be explained by the following argument. When $\theta_{i\,\max}=\theta_{RT}$, both the radiation pressure due to the incident light [34] and the amount of light reflected toward the tip are maximum (total reflection), whatever the light polarization. Thus, when $\theta_{i\,\max}=\theta_{RT}$, the interface dynamics is the fastest, as observed in Fig. 11(a).

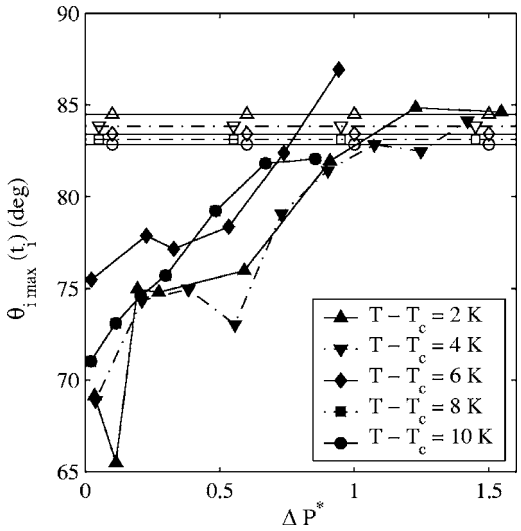

FIG. 15. Variation of the maximum value of the angle of incidence along the interface $\theta_{i\,\max}$ at the time t_i corresponding to the inflection of $h(0,t)$ [see Fig. 11(a)] as a function of the reduced distance to onset ΔP^* for several values of $T-T_c$. Lines joining experimental data are a guide for the eye. Each horizontal line decorated with open symbols indicates the value of the angle of total reflection, θ_{RT}, at the temperature corresponding to the solid symbols.

To conclude this section, we showed that the instability growth rate at time t_i of apparent instability onset is linked to the value of the maximum of the angle of incidence along the deformed interface $\theta_{i\,\max}(t_i)$—i.e., to the amount of light reflected on the interface. This is compatible with the hypothesis that the light reflected toward the hump tip is involved in the instability mechanism.

VI. CONCLUSION

We investigated the dynamics of a liquid-liquid interface when it is deformed by the radiation pressure of a focused cw Gaussian laser beam. We measured the temporal evolution of both the hump height and the hump curvature. Extending the results of Ref. [10] to the case of liquid-liquid interfaces and to the $\mathrm{Bo}\simeq 1$ regime, we showed that, in the $\mathrm{Bo}\ll 1$ and $\mathrm{Bo}\simeq 1$ ranges, the temporal evolution of the small-amplitude deformations is correctly described by a linear hydrodynamic theory predicting an overdamped dynamics. In particular, the dynamics of the hump curvature was found to be correctly predicted by the dispersion relation of plane interfacial waves Eq. (7) using $k_{\mathrm{eff}}=0.5\omega_0^{-1}$ as the effective wave number representing the hump deformation in the $\mathrm{Bo}\gg 1$ regime and up to $\mathrm{Bo}\simeq 1$. The same result was established for the dynamics of the hump height in the $\mathrm{Bo}\geqslant 10^{-2}$ regime, and a logarithmic behavior at late stage of the hump height dynamics was numerically evidenced at very small Bo number. We also investigated the dynamics of the large-amplitude interface deformations at the onset of the

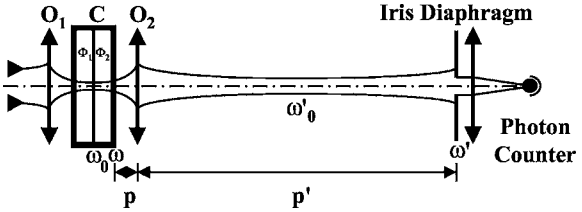

FIG. 16. Optical setup to filter and measure the beam transmitted through the hump. $O1$ and $O2$ are the microscope lenses used, respectively, to focus the laser beam on the fluid interface (beam waist ω_0) and to image the beam radius ω at the exit face of the cell C on the iris diaphragm (beam waist ω'). ω_0' is an intermediate beam waist. p (p') are the distances between the exit face of the cell and $O2$ (between $O2$ and the iris diaphragm).

optohydrodynamic instability. Using a simple, phenomenological model for the nonlinear evolution of the hump height, we interpreted the observed interface dynamics at the instability onset as the signature of an imperfect subcritical instability. Nevertheless, the actual instability mechanism remains unrevealed by the theory and shall deserve further investigation.

ACKNOWLEDGMENTS

The authors thank S. Fauve for fruitful discussion and A. Chater for his experimental contribution. They also thank M. Winckert and J. Plantard for technical assistance. This work was partly supported by Centre National de la Recherche Scientifique and Conseil Régional d'Aquitaine.

APPENDIX: RELATIONSHIP BETWEEN THE CURVATURE OF THE HUMP AND THE INTENSITY OF THE TRANSMITTED LIGHT

The determination of the hump curvature dynamics is based on the measurement of the temporal evolution of the intensity of the laser beam refracted by the hump acting as a lens. To be able to compare our beam power measurements to the predicted characteristic timescale of evolution of the hump curvature, the beam power variations have to be proportional to the hump curvature variations. In this appendix, we prove that it is effectively the case for interface deformations of curvature small enough so that the resulting focal length of the liquid lens is large compared to the path of the focused beam. The detailed optical setup used to filter and measure the beam transmitted through the hump is shown in Fig. 16. Taking into account the smallness of the beam waists used, it is not possible to directly measure the optical transmission through a diaphragm located just behind the sample. Thus, we used the microscope objective $O2$ to image the exit face of the sample cell on the iris diaphragm located at a large distance, as shown in Fig. 16. If P_i denotes the power of the TEM_{00} Gaussian beam incident to the diaphragm and P_t the transmitted beam power, the transfer function T of the diaphragm of aperture radius ρ is given by

$$T = \frac{P_t}{P_i} = 1 - \exp\left(-2\frac{\rho^2}{\omega'^2}\right), \tag{A1}$$

where ω' is the beam radius on the diaphragm. Since the distance p' between $O2$ and the iris diaphragm is large compared to the distance p between the exit face of the experimental cell and $O2$, we can approximate the Gaussian propagation laws by those of geometric optics. Then, $\omega'/\omega = p'/p$, where $\omega(z)$ is the beam radius at the exit face of the experimental cell; in our experiment, we have $z=2$ mm corresponding to 1 mm of phase Φ_2 plus 1 mm of quartz window. The transfer function becomes

$$T = 1 - \exp\left(-2\frac{\rho^2}{(p'/p)^2\omega^2}\right). \tag{A2}$$

Without any focusing effect (flat interface), the beam radius $\omega(z)_{f=\infty}$ at the exit face of the sample cell is such that

$$\omega(z)_{f=\infty}^2 = \omega_0^2\left[1 + \left(\frac{\lambda z}{\pi\omega_0^2}\right)^2\right] \tag{A3}$$

in the paraxial ray approximation, where ω_0 is the beam waist at the interface ($z=0$). Besides, when the interface is deformed and gives birth to a thin lens of focal distance f, the expression of the beam radius $\omega(z)_f$ at the exit face of the cell is

$$\omega(z)_f^2 = \omega_0^2\left[\left(1 - \frac{z}{f}\right)^2 + \left(\frac{\lambda z}{\pi\omega_0^2}\right)^2\right]. \tag{A4}$$

Experimentally, we considered a situation where $z<f$ in order to investigate the dynamics of the interface in the linear regime in deformation. Moreover, we choose $\rho/\omega' < 1$ to work in the paraxial-ray approximation where the interface deformation can be assimilated to a thin spherical lens. In these conditions, we get

$$T(\omega(z)_f) \approx T(\omega(z)_{f=\infty})\left[1 + 2\left(\frac{\omega_0}{\omega(z)_{f=\infty}}\right)^2\frac{z}{f}\right]. \tag{A5}$$

Note that both ω_0 and z are fixed in a given experiment, so that the only, time-dependent variable is f. Finally, in the paraxial-ray approximation, f is given by [35]

$$\frac{1}{f} = \frac{n_2 - n_1}{2n_2}\kappa(0,t), \tag{A6}$$

where $\kappa(0,t)$ is the curvature of the interface on the beam axis at time t. This leads to

$$T(\omega(z)_{f(t)}) \simeq T(\omega(z)_{f=\infty})[1 + \alpha\kappa(0,t)], \tag{A7}$$

where α is a constant. Consequently, the beam power transmitted through the iris diaphragm is an affine function of $\kappa(0,t)$. Assuming $\kappa(0,t) = \kappa(0,\infty)[1 - \exp(-t/\tau_{\text{eff}})]$, we finally find

$$T(\omega(z)_{f(t)}) \simeq T(\omega(z)_{f=\infty})\{1 + \alpha\kappa(0,\infty)[1 - \exp(-t/\tau_{\text{eff}})]\}, \tag{A8}$$

where τ_{eff} is the characteristic time scale of the linear interface deformation. The fit of the example of temporal behavior of the transmission presented in the inset of Fig. 9 by the predicted expression, Eq. (A8), shows good agreement.

[1] A. Ashkin and J. M. Dziedzic, Phys. Rev. Lett. **30**, 139 (1973).
[2] J. Z. Zhang and R. K. Chang, Opt. Lett. **13**, 916 (1988).
[3] I. I. Komissarova, G. V. Ostrovskaya, and E. N. Shedova, Opt. Commun. **66**, 15 (1987).
[4] A. Casner and J. P. Delville, Opt. Lett. **26**, 1418 (2001).
[5] A. A. Kolomenskii and H. A. Schuessler, Appl. Opt. **38**, 6357 (1999).
[6] J. P. Longtin, K. Hijikata, and K. Ogawa, Int. J. Heat Mass Transfer **42**, 85 (1999).
[7] J. C. Loulergue, Y. Lévy, and C. Imbert, Opt. Commun. **45**, 149 (1983).
[8] S. A. Viznyuk, P. P. Pashinin, and A. T. Sukhodol'skii, Opt. Commun. **85**, 254 (1991).
[9] K. Sakai, K. Tachibana, S. Mitani, and K. Takagi, J. Colloid Interface Sci. **264**, 446 (2003).
[10] Y. Yoshitake, S. Mitani, K. Sakai, and K. Takagi, J. Appl. Phys. **97**, 024901 (2005).
[11] A. Casner and J. P. Delville, Phys. Rev. Lett. **87**, 054503 (2001).
[12] R. Wunenburger, A. Casner, and J. P. Delville, preceding paper Phys. Rev. E **73**, 036314 (2006).
[13] H. M. Lai, P. T. Leung, K. L. Poon, and K. Young, J. Opt. Soc. Am. B **6**, 2430 (1989).
[14] I. Brevik and R. Kluge, J. Opt. Soc. Am. B **16**, 976 (1999).
[15] A. Hallanger, I. Brevik, S. Haaland, and R. Sollie, Phys. Rev. E **71**, 056601 (2005).
[16] A. M. Gañan-Calvo, J. Dávila, and A. Barrero, J. Aerosol Sci. **28**, 249 (1997).
[17] R. Badie and D. Frits de Lange, Proc. R. Soc. London, Ser. A **453**, 2573 (1997).
[18] B. Jean-Jean, E. Freysz, A. Ducasse, and B. Pouligny, Europhys. Lett. **7**, 219 (1986).
[19] G. V. Ostrovskaya, Sov. Phys. Tech. Phys. **33**, 465 (1988).
[20] G. B. Arfken and H. J. Weber, *Mathematic Methods for Physicists*, 4th ed. (Academic, New York, 1995).
[21] V. G. Levich, *Physiochemical Hydrodynamics* (Prentice Hall, London, 1962), Sec. 117.
[22] H. Lamb, *Hydrodynamics*, 6th ed. (Cambridge University Press, Cambridge, England, 1997), Chap. XI, p. 349.
[23] M. S. Plesset and C. G. Whipple, Phys. Fluids **17**, 1 (1974).
[24] J. L. Harden, H. Pleiner, and P. A. Pincus, J. Chem. Phys. **94**, 5208 (1991).
[25] As a matter of fact, Eq. (7) can be solved analytically in its polynomial form involving the variable A—i.e., by determining the roots of the denominator of the last term of the integrand in Eq. (4).
[26] E. Freysz, Ph.D. thesis, No. 976, Bordeaux I University, 1990.
[27] K. Sakai, D. Mizuno, and K. Takagi, Phys. Rev. E **63**, 046302 (2001).
[28] This is linked to a classical problem of convergence of the diffusion equation in cylindrical geometry [see, for instance, J. P. Gordon *et al.* J. Appl. Phys. **36**, 3 (1965)]. As far as we consider a boundary condition at infinity, the gradient in height approaches $1/r$ in the steady state, and with the boundary condition $h(r=\infty,t)=0$, the height integrates to infinity at all finite radii. That is why we took a finite boundary condition [$h(r=\omega_{bc,t=\infty})$] to find the stationary solution [12].
[29] B. Jean-Jean, E. Freysz, A. Ponton, A. Ducasse, and B. Pouligny, Phys. Rev. A **39**, 5268 (1989).
[30] A. Casner and J. P. Delville, Phys. Rev. Lett. **90**, 144503 (2003).
[31] A. Casner and J. P. Delville, Europhys. Lett. **65**, 337 (2004).
[32] J. C. Bacri and D. Salin, J. Magn. Magn. Mater. **39**, 48 (1983).
[33] P. Manneville, *Structures Disspatives Chaos et Turbulence* (CEA, Saclay, 1991).
[34] A. Casner, J. P. Delville, and I. Brevik, J. Opt. Soc. Am. B **20**, 2355 (2003).
[35] M. Born and E. Wolf, *Principles of Optics*, 6th ed. (Pergamon, Oxford,1980).